

Electronic Supplementary Information

A single-site iron catalyst with preoccupied active center that achieves selective ammonia electrosynthesis from nitrate

Panpan Li,^a Zhaoyu Jin,^{b*} Zhiwei Fang,^a and Guihua Yu^{a*}

Experimental details and calculations

SI-SECM measurements

Surface interrogation scanning electrochemical microscope (SI-SECM) analysis was conducted on a CHI920C SECM bipotentiostat (CH Instrument, the USA). As shown in Fig. 3a, a typical SI-SECM setup includes two identical aligned ultramicroelectrodes (UMEs) named tip UME (at the top) and substrate UME (at the bottom), which is placed in a faraday cage on a vibration isolation table. UMEs were prepared by tightly sealing a platinum wire (50 μm in diameter) in a glass tube with an RG (radius of metal electrode/radius of the glass sheath) value of 1.5-2.0. The substrate UME was fixed at the bottom of the electrolytic cell, while the tip UME can be freely moved to X, Y, Z direction via a positioner.¹ To load catalysts, a cavity (diameter: 50 μm ; depth: 2-3 μm) was created by electrochemically etching the substrate UME in CaCl_2 aqueous solutions according to the previous report.² Fe-PPy SACs and Fe NPs powders were then pressed in the cavity to closely contact with Pt for better electric conduction. The alignment of tip and substrate UMEs can be determined by the positive feedback approaching curve in the solution containing 0.5 mM ferrocenemethanol (FcMeOH) and 0.1 M KOH. Specifically, the tip was hold at the potential of FcMeOH oxidation (1.4 V vs. RHE) and approached to the substrate that was also applied the potential to reduce FcMeOH⁺ (1.0 V vs. RHE) with the assistance of an optical microscope. The tip current (i_{tip}) was recorded with the traveling distance (d) and a positive feedback could be observed because of the cycling of the redox species (FcMeOH/FcMeOH⁺) between the electrodes. After adjusting X and Y directions to obtain the highest feedback i_{tip} , we further moved the tip along Z direction by using a piezo block positioner with a rate of 0.2 $\mu\text{m s}^{-1}$. The plots of i_{tip} vs. d normalized by the tip current at infinity (i_{inf}) and the radius of the tip (a) were fitted with a theoretical positive feedback curve to obtain the exact inter-electrode distance.^{1,3} In all SI-SECM experiments, the inter-electrode distance was controlled at ca. 2 μm with the theoretical fitting curve as indicated in Fig. S14b, where the tip could fully collect the feedback species from the substrate. For determining Fe contents on catalysts, the substrate UME was first applied the given potentials (1.2 to -0.2 V vs. RHE) for 20 s to produce active Fe sites (Fe(II) or Fe(0)). Subsequently, the chronoamperogram of the tip at 1.4 V vs. RHE was recorded, during which tip-generated FcMeOH⁺ would rapidly react with Fe(II) (or Fe(0)) on the substrate UME. A positive feedback was expected to be seen on the tip current until all Fe(II) or Fe(0) species on the substrate were totally consumed. The number of charges (Q_{tip}) was calculated by the integration of i_{tip} -

t curves at different substrate potentials with the background subtraction of negative feedback (Q_{tip} at $E_{sub} = 1.2$ V).

Determination of NO_2^- using the Griess test

After chronoamperometry tests, NO_2^- in electrolyte was determined by Griess test.⁴ The Griess agent was prepared by dissolving N-(1-naphthyl)ethyldiamine dihydrochloride (0.8 g), sulfonamide (0.04 g) and H_3PO_4 (2 mL, 85%) into 10 ml of DI water. Before the analysis, the nitrite-containing electrolyte (0.1 M KOH) was diluted to the neutral state using HCl (0.1 M). Then, diluted solutions (2 mL) were mixed with the Griess agent (40 μ L) and rested for 10 min at room temperature. UV-Vis spectrophotometer was employed to record absorption spectrum (400-650 nm) and the absorbance at ca. 540 nm was used to determine the concentration of generated NO_2^- . The calibration curve was obtained by using various $NaNO_2$ aqueous solutions as the standard samples (Fig. S6d) in the same operation.

Determination of NH_3 using the indophenol blue method

The produced NH_3 was determined by the indophenol blue method.⁵ Specifically, the target solution (1 mL) was moved into a clean vessel (5 mL) followed by sequentially adding NaOH solution (1 mL, 1 M) containing salicylic acid (5 wt%) and sodium citrate (5 wt%), NaClO (0.5 mL, 0.05 M), and $Na[Fe(NO)(CN)_5]$ (0.1 mL, 1wt%) aqueous solution. After the incubation for 2 h at room temperature, the mixture was subjected to UV-Vis measurements and resulted in the absorption spectrum (ranged from 500-800 nm). The absorption peak at 655 nm was ascribed to the generated indophenol blue originated from NH_3 in the target solution. To accurately quantify NH_3 , concentration-absorbance curves were calibrated using a series of standard ammonia chloride in KOH solutions (0.1 M) (Fig. S6a). The absorbance of the blank sample without adding the standard NH_3 solution was subtracted from the measured peak absorbance of all tested samples for background correction.

Determination of NH_3 using the 1H NMR spectroscopy

The amount of produced NH_3 was also quantified by the 1H NMR spectroscopy. After chronoamperometry tests in Ar-saturated 0.1 M KOH containing 0.1 M KNO_3 at -0.6 V vs. RHE for 0.5 h, the electrolyte (50 μ L, 5 mL electrolytes in total) in the cathodic chamber was neutralized by H_2SO_4 aqueous solution (50 μ L, 0.05 M). After that, the neutralized electrolyte (30 μ L) was mixed with maleic acid (as the internal standard) aqueous solution (10 μ L, 3.6 mM), H_2SO_4 aqueous solution (10 μ L, 4 M), and d^6 -DMSO (550 μ L). After adding tetramethylsilane as the reference, the mixture was sealed into an NMR tube (5 mm in diameter, 600 MHz) for further tests. All 1H NMR tests were conducted with water suppression using the presaturation experiment. The concentration of produced NH_3 can be determined by comparing the integral area (I) of the vinylic singlets for maleic acid (6.25 ppm, 2H) and the typical triplet for ammonium (7.18 ppm, 4H, J = 52 Hz) based on the followed equation.

$$C_{NH_4^+} = \frac{I_{NH_4^+}/H_{NH_4^+}}{I_s/H_s} \times C_s \quad (1)$$

, where $C_{NH_4^+}$ and C_s are the concentration of ammonium and maleic acid (60 μ mol L^{-1}) in NMR tubes; $H_{NH_4^+}$ and H_s are the number of protons for ammonium and maleic acid; $I_{NH_4^+}$ and I_s are

the integrals of ^1H NMR peaks for ammonium and maleic acid. Considering the dilution, the calculated $C_{\text{NH}_4^+}$ needs to multiply by 40 to give the real concentration of produced NH_3 . The isotopic labeling experiment was conducted to confirm the origin of ammonium using Ar-saturated 0.1 M KOH containing K^{15}NO_3 as the electrolyte in the same operation described above.

The produced NH_4^+ (in μmol , Fig. S10b) was determined to be:

$$M_{\text{NH}_4^+} = C_{\text{NH}_4^+} \times 40 \times 5 \text{ mL} \quad (2)$$

Determination of H_2 using SECM

The amount of hydrogen determined with the SECM was carried out under the same conditions with the bulk electrolysis as described above. Briefly, a Pt UME as the H_2 probe was placed above the carbon fiber paper electrode loaded with catalysts. A typical substrate-generation tip-collection mode was employed and the distance between the Pt UME and the catalysts was controlled at 15 μm for all of the measurements. Modeling based on finite element analysis was carried out for calibrations of the distance and the concentration profile of H_2 generated by substrate catalysts as shown in Fig. S8.⁶

Calculation of the yield rate and the faradaic efficiency of NH_3

The yield rate (Y.R., $\text{mg}_{\text{NH}_3} \text{h}^{-1} \text{cm}^{-2}$) of NH_3 can be calculated using the following equation:

$$\text{Y.R.}(\text{NH}_3) = (C_{\text{NH}_3} \times V)/(t \times A) \times 10^{-3} \quad (3)$$

The faradaic efficiency (F.E.) of NH_3 was the percentage of the charge consumed for NH_3 generation in the total charge passed through the electrode according to the equation below:

$$\text{F.E.}(\text{NH}_3) = (8 \times F \times C_{\text{NH}_3} \times V \times 10^{-6})/(17 \times Q) \times 100\% \quad (4)$$

where C_{NH_3} is the measured NH_3 concentration ($\mu\text{g mL}^{-1}$); V is the volume of the electrolyte (30 mL); t is the electrolysis time (0.5 h); A is the geometric area of the electrode (0.25 cm^2); F is the faraday constant (96485 C mol^{-1}); Q (C) is the total charge passed through the electrode, which is the integral of I - t curve. The yield rate, the faradaic efficiency, and corresponding error bars were obtained from three individual samples under the same testing conditions.

The faradaic efficiency of NO_2^- , H_2 , and other products

The faradaic efficiency of NO_2^- was the percentage of the charge for producing NO_2^- in the total charge (Q) recorded by I - t curve according to the equation below:

$$\text{F.E.}(\text{NO}_2^-) = (2 \times F \times C_{\text{NO}_2^-} \times V \times 10^{-6})/(46 \times Q) \times 100\% \quad (5)$$

, where $C_{\text{NO}_2^-}$ is the measured NO_2^- concentration ($\mu\text{g mL}^{-1}$).

The faradaic efficiency of H_2 , $\text{F.E.}(\text{H}_2)$, can be simply calculated according to the probe and electrolytic currents before and after the addition of NO_3^- , assuming 100% $\text{F.E.}(\text{H}_2)$ in the solution with nitrate free.

$$\text{F.E.}(\text{H}_2) = (i_{\text{probe, w/ Nit.}} / i_{\text{probe, w/o Nit.}}) \times (i_{\text{cat., w/o Nit.}} / i_{\text{cat., w/ Nit.}}) \times 100\% \quad (6)$$

, where $i_{\text{probe, w/ Nit.}}$ and $i_{\text{probe, w/o Nit.}}$ are the probe currents with and without adding NO_3^- ; $i_{\text{cat., w/o Nit.}}$ and $i_{\text{cat., w/ Nit.}}$ present the catalytic currents on substrate catalysts with and without NO_3^- .

The faradaic efficiency of other products (e.g. N_2 , N_2H_4 , NO_2 etc.) was the remaining

percentage apart from F.E.(NH₃), F.E.(NO₂⁻), and F.E.(H₂) based on the equation:

$$F.E.(others) = 100\% - F.E.(NH_3) - F.E.(NO_2^-) - F.E.(H_2) \quad (7)$$

The energy consumption for producing NH₃

For electrocatalytic ammonia synthesis (NitRR and N₂RR), the energy consumption (E.C., kWh kg_{NH₃}⁻¹) was obtained assuming the overpotential of the water oxidation at anode is zero.

$$E.C.(NH_3) = n \times F \times (1.23 - E) / (3600 \times 17) \quad (8)$$

, where n is the electron number for producing ammonia (8 for NitRR and 3 for N₂RR); E is the applied potential (vs. RHE) for NH₃ production.

For photocatalytic ammonia synthesis, E.C. (kWh kg_{NH₃}⁻¹) was determined according to the equation:

$$E.C.(NH_3) = P_r \times A_r / (Y.R. \times m) \quad (9)$$

, where P_r is the radiation power (W cm⁻²); A_r is the radiation area (cm²); Y.R. is the yield rate (kg_{NH₃} h⁻¹ g⁻¹); m is the total mass of catalysts (g).

The half-cell energy efficiency for producing NH₃

Assuming the overpotential of anodic electrode (the water oxidation) is zero, the half-cell energy efficiency (E.E.) defined as the ratio of chemical energy to applied electrical power was calculated with the following equation:

$$E.E.(NH_3) = (1.23 - E_{NH_3^0}) \times F.E.(NH_3) / (1.23 - E) \times 100\% \quad (10)$$

, where E_{NH₃}⁰ is the equilibrium potential (0.70 V) of nitrate electroreduction to ammonia in alkaline media; F.E.(NH₃) is the faradaic efficiency for NH₃; 1.23 V is the equilibrium potential of water oxidation (i.e. assuming the overpotential of the water oxidation is zero); E is the applied potential (vs. RHE) for NH₃ production.

For photocatalytic ammonia synthesis, the energy efficiency is equivalent to the quantum efficiency.

The calculation of electrochemical active surface area

The electrochemical active surface area (A_{EASA}) of catalysts loaded on the UME (A_{EASA,UME}, μm²) and carbon fiber paper (A_{EASA,CFP}, μm² cm_{geo}⁻²) was based on the ideal specific capacitance of carbon electrode (C_{EDLC,carbon} = 10 μF cm⁻²) and metal electrode (C_{EDLC,metal} = 30 μF cm⁻²) according to the following equation:

$$A_{EASA} = C_{EDLC} / C_{EDLC,carbon} \text{ (or } C_{EDLC,metal}) \quad (11)$$

, where C_{EDLC} is the electric double-layer capacitance of catalysts and is determined by CVs at various scan rates (Fig. S15).

The calculation of EASA-based site density

The EASA-based site density (atom μm_{EASA}⁻²) was calculated according to titrated site numbers and A_{EASA,UME} of catalysts loaded on the UME shown as below.

$$D_{\text{site density}} = \frac{(C_x - C_{1.2}) \times 10^6}{n \times A_{EASA,UME} \times F} \times N_A \quad (12)$$

, where C_x and $C_{1,2}$ are the integrated charge (nC) from titration curves at a specific substrate potential (x) and 1.2 V (as the background); n is the number of electrons for oxidizing Fe species (3 for Fe(0), 1 for Fe(II)); A_{EASA} is electrochemical active surface area of catalysts on the UME determined by equation (11); F is faradic constant (96485 C mol^{-1}); N_A is the Avogadro constant (6.02×10^{23}).

Turnover frequency of ammonia

Turnover frequency (TOF, s^{-1}) of ammonia in NitRR process indicates the number of ammonia molecules produced per unit time and per active sites. Thus, TOF values can be calculated based on the yield rate (Y.R.(NH₃), $\text{mg}_{\text{NH}_3} \text{ h}^{-1} \text{ cm}^{-2}$) and EASA-based site density ($D_{\text{site density}}$, $\text{atom } \mu\text{m}_{EASA}^{-2}$) as followed.

$$\text{TOF} = \frac{\text{Y.R.}(\text{NH}_3) \times N_A}{D_{\text{site density}} \times A_{EASA,CFP} \times 17 \times 3600} \quad (13)$$

Reaction rate constant

A pseudo-first order rate constant can be confirmed by varying delay time (t_{delay}) for generating the titrant (FcMeOH^+) on the tip UME. During t_{delay} , the produced Fe active sites (Fe(0) at -0.2 V, Fe(II) at 0.2 V) on the substrate UME could mainly react with NO_3^- in 0.1 M KOH electrolytes with adding 0.1 M KNO_3 , while they could react with H_2O for producing H_2 without KNO_3 . After t_{delay} , FcMeOH^+ was generated to oxidize the remaining Fe active sites. Therefore, Fe species consumed by NO_3^- and H_2O related to t_{delay} can be plotted to determine the reaction rate constant of NO_3^- ($k_{\text{NO}_3^-}$) and H_2O adsorption ($k_{\text{H}_2\text{O}}$).

In 0.1 M KOH containing KNO_3 , the NO_3^- adsorption process is described below.



In 0.1 M KOH without KNO_3 , the adsorption process on Fe sites is expressed as follows.



In this system, NO_3^- and H_2O contents are almost unchanged and are also much higher than Fe active sites. Thus, these adsorption processes can be considered as a pseudo-first order reaction.

In 0.1 M KOH + 0.1 M KNO_3 , $k_{\text{NO}_3^-}$ can be determined by plotting $\ln[\text{Fe}]$ as a function of t_{delay} .

$$-\frac{d[\text{Fe}]}{dt_{\text{delay}}} = k_{\text{NO}_3^-} \times [\text{Fe}] \quad (16)$$

$$\ln [\text{Fe}]_{t_{\text{delay}}} = -k_{\text{NO}_3^-} \times t_{\text{delay}} + \ln[\text{Fe}]_0 \quad (17)$$

, where $[\text{Fe}]$ ($\mu\text{mol cm}_{EASA}^{-2}$) is surface concentration of Fe active sites ($[\text{Fe}] = D_{\text{site density}}/N_A$) at

the delay time.

Similarly, in 0.1 M KOH without KNO₃, $k_{\text{H}_2\text{O}}'$ can be calculated according to the following equation.

$$-\frac{d[\text{Fe}]}{dt_{\text{delay}}} = k_{\text{H}_2\text{O}}' \times [\text{Fe}] \quad (18)$$

$$\ln [\text{Fe}]_{t_{\text{delay}}} = -k_{\text{H}_2\text{O}}' \times t_{\text{delay}} + \ln[\text{Fe}]_0 \quad (19)$$

Through plotting [Fe] against t_{delay} , $k_{\text{NO}_3^-}'$ and $k_{\text{H}_2\text{O}}'$ can be calculated according to the slopes of the linear fitting results as shown on Fig. 3c and d.

Density functional theory (DFT) calculations

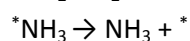
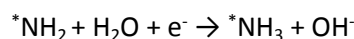
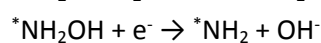
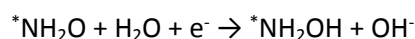
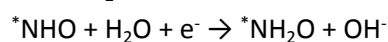
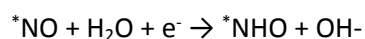
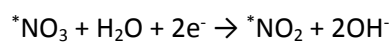
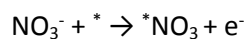
All DFT calculations in this study were performed using DMOL³ code with Perdew-Burke-Ernzerhof (PBE) functional and the plane-wave pseudopotential for the spin-polarized generalized gradient approximation (GGA).^{7, 8} The empirical DFT-D method with the Grimme scheme was applied for dispersion corrections, including van der Waals interactions.^{9, 10} One Fe-N₄ moiety was anchored onto the center of 6 × 6 graphene monolayer separated by a vacuum layer of 20 Å. The process of geometry optimization approached the convergence criteria for the energy and force on each atom reducing below 1 × 10⁻⁶ eV and 0.01 eV Å⁻¹. The real-space global orbital cutoff radius was set to 4.7 Å with a 3 × 3 × 1 *k*-point grid for all calculations.

The conductor-like screening model (COSMO) was employed to introduce the treatment of solvation effects.^{11, 12} The free energy (ΔG) calculations of each elementary step were based on the standard hydrogen electrode model, which can be determined as¹³

$$\Delta G = \Delta E + \Delta E_{\text{ZPE}} - T\Delta S - neU \quad (20)$$

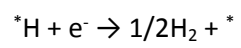
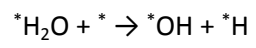
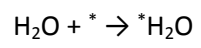
where ΔE and ΔS are the reaction energy and entropy change; ΔE_{ZPE} is the difference in zero-point energy between the adsorbed and the gas phase molecules; U is the applied bias and n is the electron transfer number involved in the reaction. Here $U = 0$ V for free energies diagrams demonstrated in the paper.

Element steps of nitrate reduction on Fe-based catalysts were simulated according to the following reactions:



where * represents the adsorption site. And similarly, the hydrogen evolution reaction was

also simulated as the following steps:



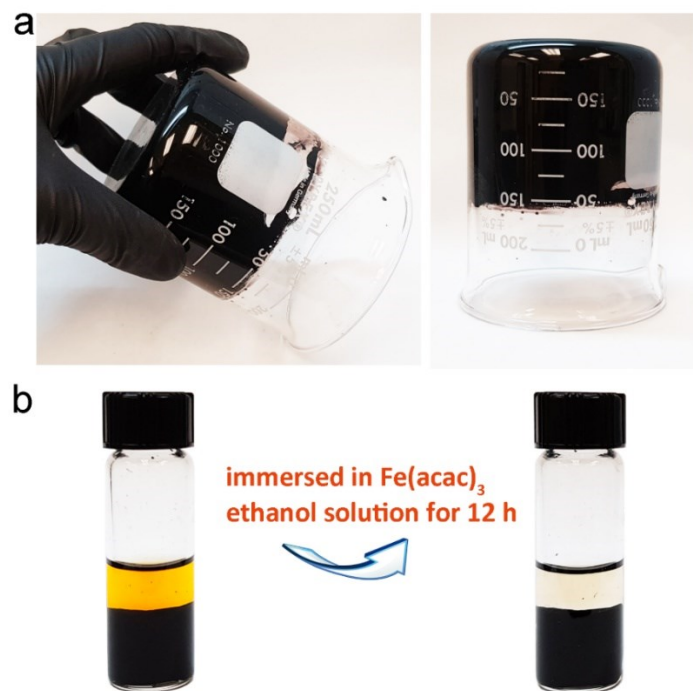


Fig. S1 Photos of PPy-SDS hydrogels (a) and $\text{Fe}(\text{acac})_3$ -loaded PPy-SDS hydrogels (b).

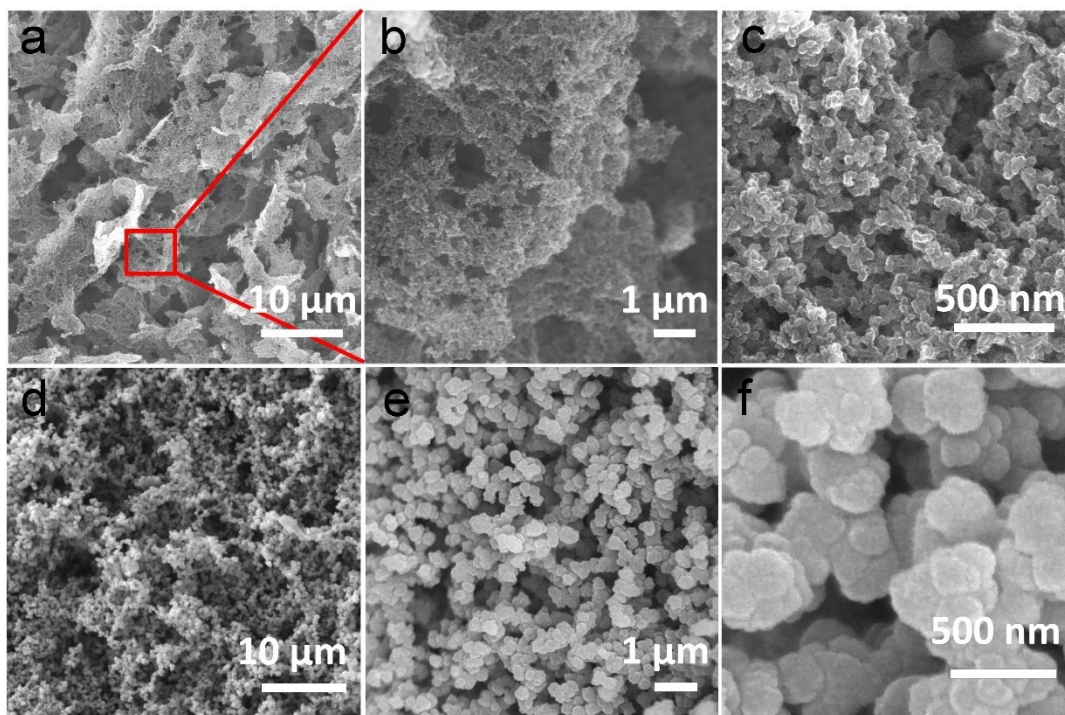


Fig. S2 SEM images of PPy-SDS hydrogels (a-c) and PPy samples (d-f) without adding SDS.

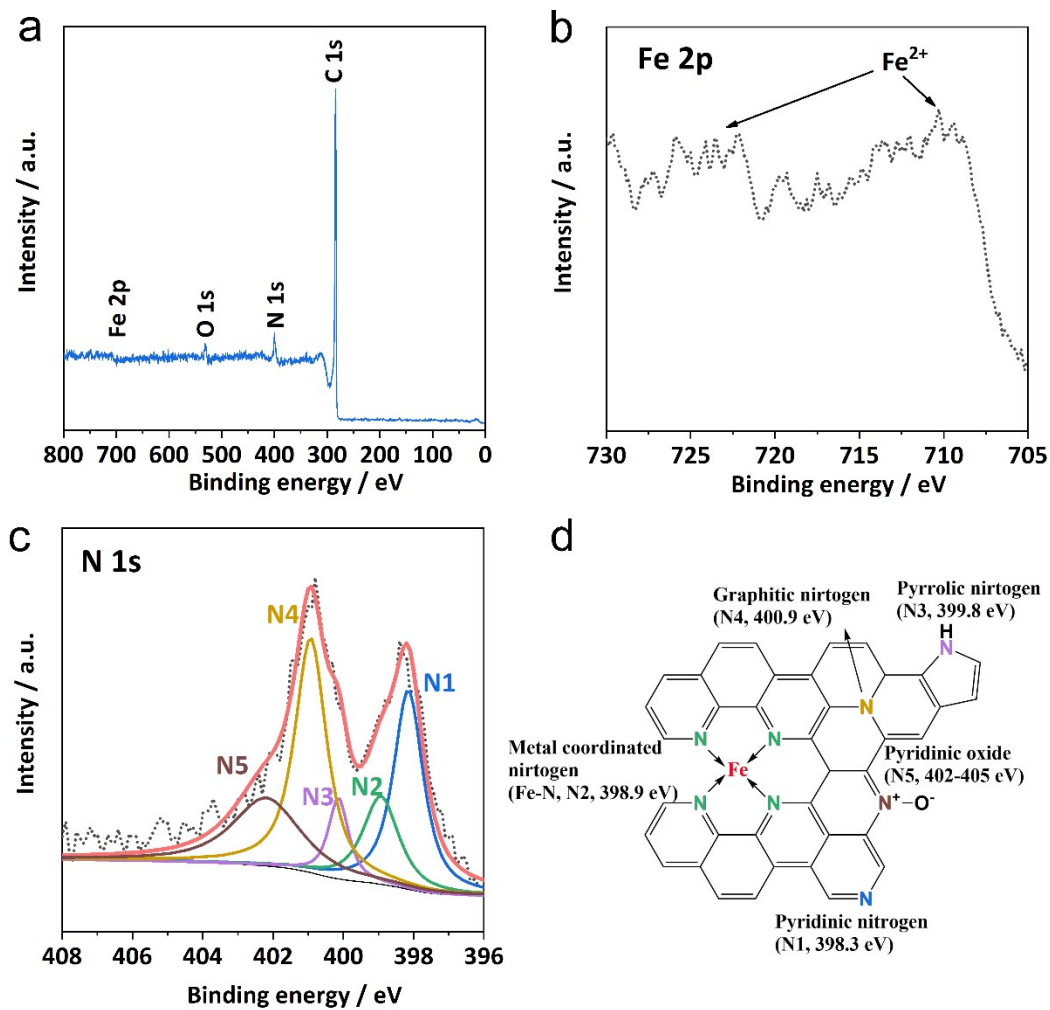


Fig. S3 XPS analysis of Fe-PPy SACs. (a) XPS survey spectrum; (b) Fe 2p spectrum; (c) N 1s spectrum; (d) chemical structures of nitrogen species on a carbon substrate.

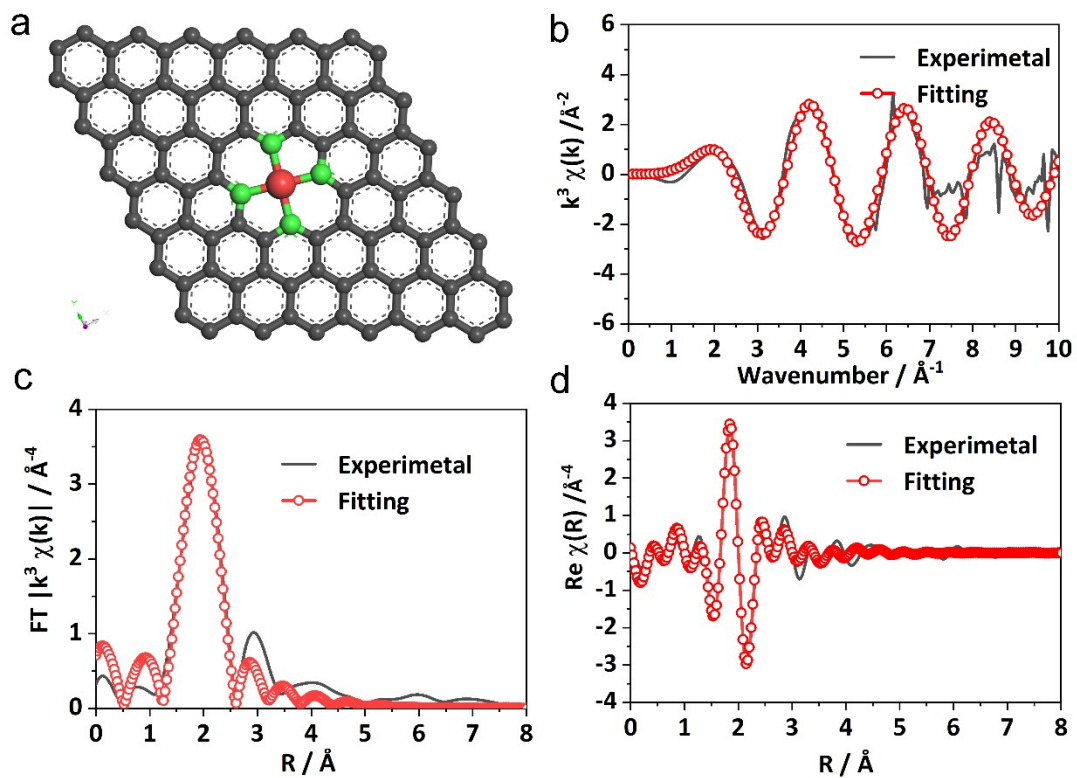


Fig. S4 (a) The optimized Fe-N4 structure. (b) The fitting curve of Fe K-edge EXAFS spectra of Fe-PPy SACs in k (b) and R space (c, d).

Table S1. First-shell fitting parameters of Fe K-edge EXAFS for Fe-PPy SACs.

Bonding mode	Fe-N
CN	3.76±0.84
R / Å	1.980±0.076
$\sigma^2 / \times 10^{-3}$	5.93±3.6
$\Delta E^0 / \text{eV}$	-2.319±1.923
k-range	1.85 - 7.1
R-range	0.6 - 2.4
R factor	0.00884

CN: coordination number;

R: the distance between absorber and backscatter atoms (or the bond length of Fe-N);

σ^2 : the Debye-Waller factor value;

ΔE^0 : the inner potential correction to account for the difference in the inner potential between the sample and the reference compound.

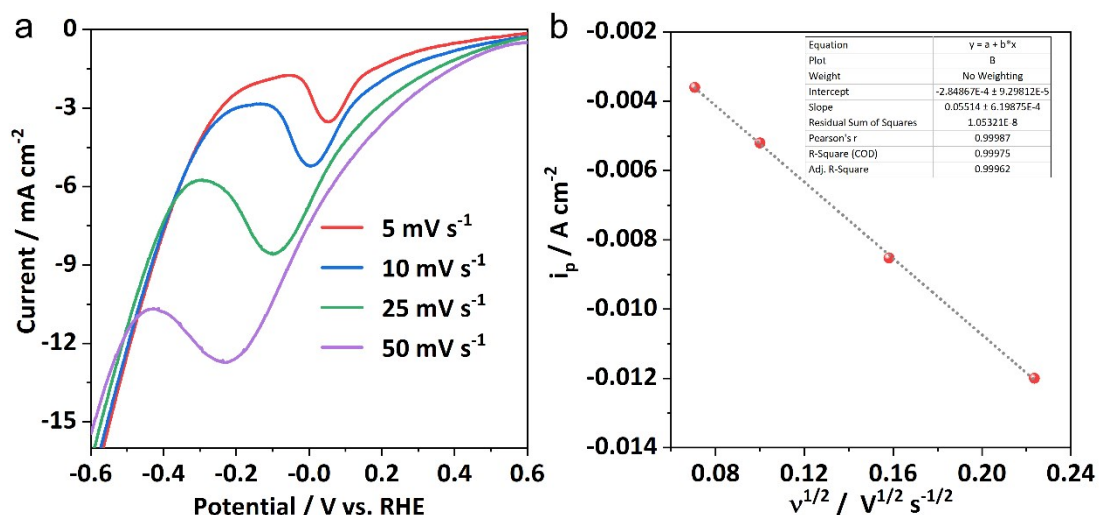


Fig. S5 (a) LSV curves of Fe-PPy SACs in 0.1 M KOH containing 10 mM KNO₃. (b) The plot of the square root of scan rate (v , V s⁻¹) vs. reduction peak current density (i_p , A cm⁻²).

Charge transfer number (n) of the reduction peak (from 0 to -0.2 V) is determined by the relationship between the peak current and the scan rate according to the Nicholson-Shain equation under a low NO₃⁻ concentration (10 mM, a diffusion-control condition),¹⁴⁻¹⁶

$$i_p = -2.99 \times 10^5 \times n \times \alpha^{1/2} \times C \times D^{1/2} \times v^{1/2}$$

, where α (ca. 0.5) is transfer coefficient; C (1×10^{-5} mol cm⁻³) is NO₃⁻ concentration in bulk electrolytes; D (2×10^{-5} cm² s⁻¹) is the diffusion coefficient.

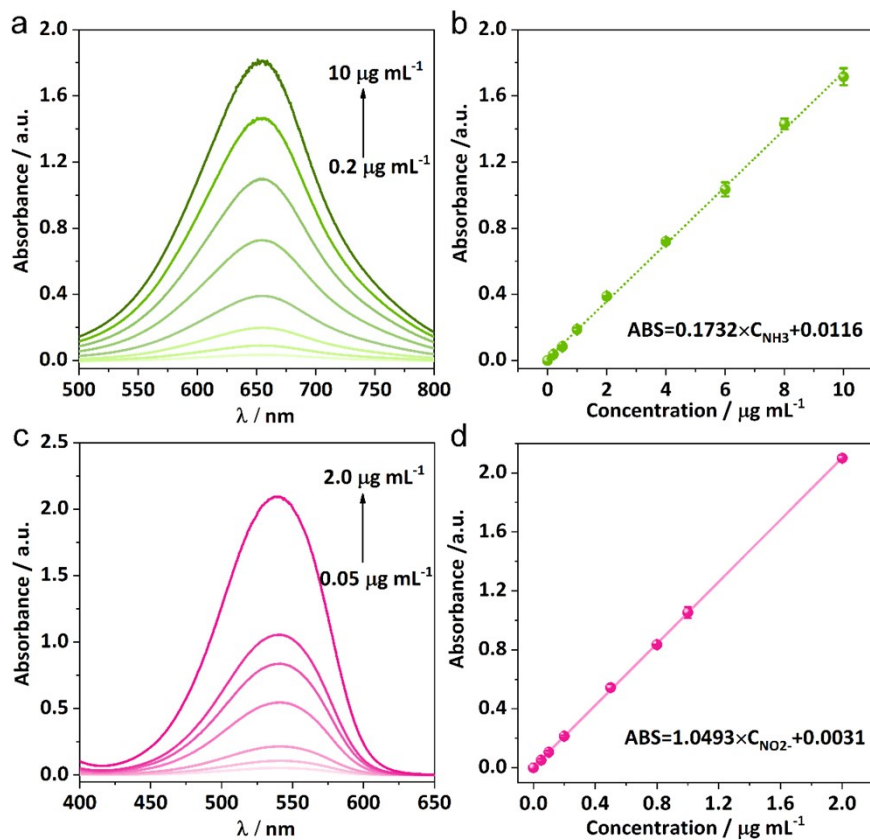


Fig. S6 UV-Vis curves and calibration curves for determining NH_3 (a, b) and NO_2^- (c, d).

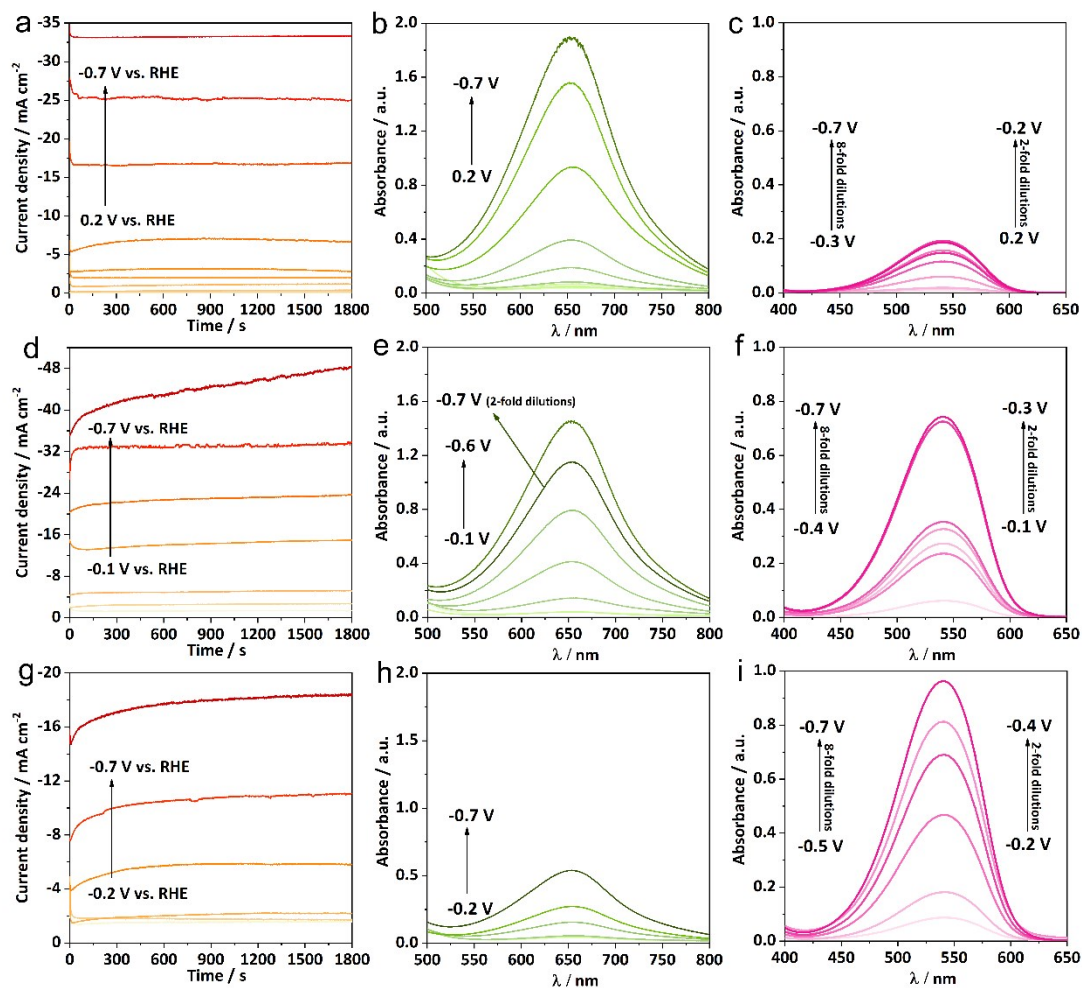


Fig. S7 I-t curves and UV-Vis curves for quantifying the efficiency of ammonia and nitrite production at various potentials. (a-c) Fe-PPy SACs; (d-f) Fe NPs; (g-i) PPy.

UV-Vis curves for a series of NH_4NO_3 standard samples ($0.2\text{--}10\ \mu\text{g mL}^{-1}$) were analyzed in Fig. S6a and the maximum absorption peak at ca. 650 nm was applied to plot the linear calibration curve (Fig. S6b) for the ammonia quantification. I-t curves (Fig. S7a) of Fe-PPy SACs at various given potentials were obtained to calculate the total charge (Q) passing through the electrode. After 30 min of electrolysis, UV-Vis spectra (Fig. S7b) were recorded to determine the concentration of generated ammonia in electrolytes according to the calibration curve.

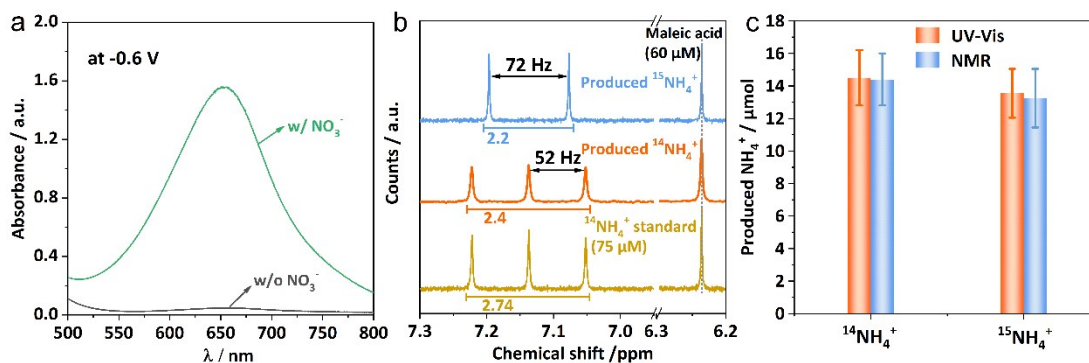


Fig. S8 (a) UV-Vis spectra of electrolytes with and without NO_3^- after 0.5 h electrolysis on Fe-PPy SACs. (b) ^1H NMR tests of produced ammonia using K^{14}NO_3 and K^{15}NO_3 as nitrogen sources. (c) The quantification of ammonia via UV-Vis and NMR measurements.

To eliminate the interference of N from the environment and catalyst, we recorded the UV-Vis spectra of electrolytes in the absence of NO_3^- after 0.5 h electrolysis with Fe-PPy SACs as shown in Fig. S8a. There is negligible ammonia detected in this test, while electrolytes with NO_3^- reveals the remarkable absorption intensity, suggesting the NO_3^- -to- NH_3 production ability on Fe-PPy SACs. We have also conducted ^{15}N labeling ^1H NMR tests to confirm this result. $^{14}\text{NO}_3^-$ was replaced by $^{15}\text{NO}_3^-$ as the N source and maleic acid (60 μM , a singlet at ca. 6.24 ppm) was employed as an internal standard for quantifying the generated ammonia (see more details in Supporting Information). From 7.05 to 7.25 ppm (Fig. S8b), $^{14}\text{NH}_4^+$ shows a typical triplet with a coupling constant of ca. 52 Hz, while $^{15}\text{NH}_4^+$ owns a characteristic doublet with ca. 72 Hz. As a result, the amount of $^{15}\text{NH}_4^+$ (ca. 13.25 μmol) is very close to that of $^{14}\text{NH}_4^+$ (ca. 14.40 μmol), implying the generated ammonia is mainly from the electrocatalytic NO_3^- -to- NH_3 reduction. Moreover, the detected ammonia via ^1H NMR is comparable to the results from UV-Vis, suggesting the indophenol blue spectrophotometry is a reliable method for determining ammonia.

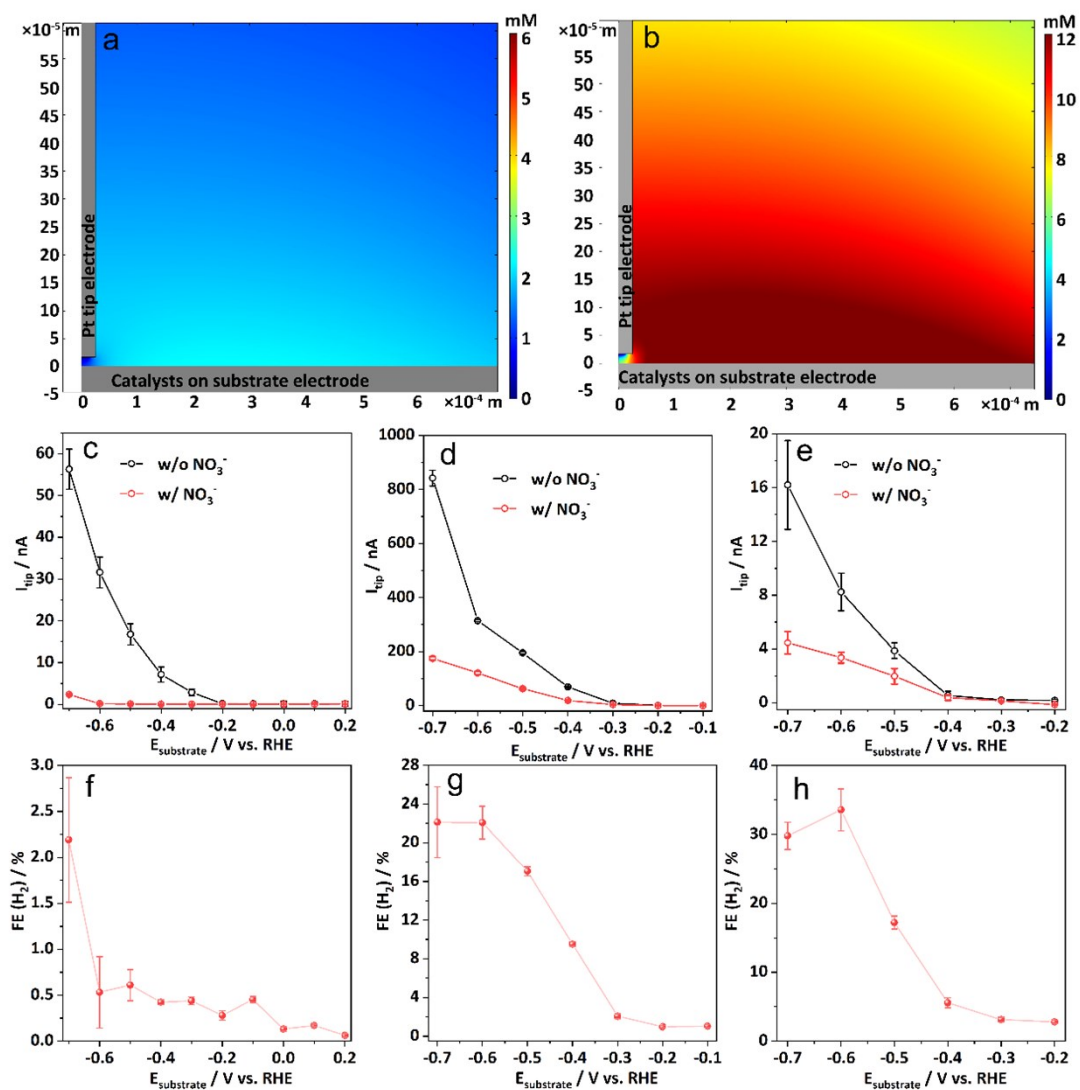


Fig. S9 The quantification of H₂ during the electrolysis. The H₂ concentration profile with (a) and without (b) adding KNO₃. The substrate generation-tip collection tests for detecting H₂ on Fe-PPy SACs (c, f), Fe NPs (d, g), and PPy (e, h).

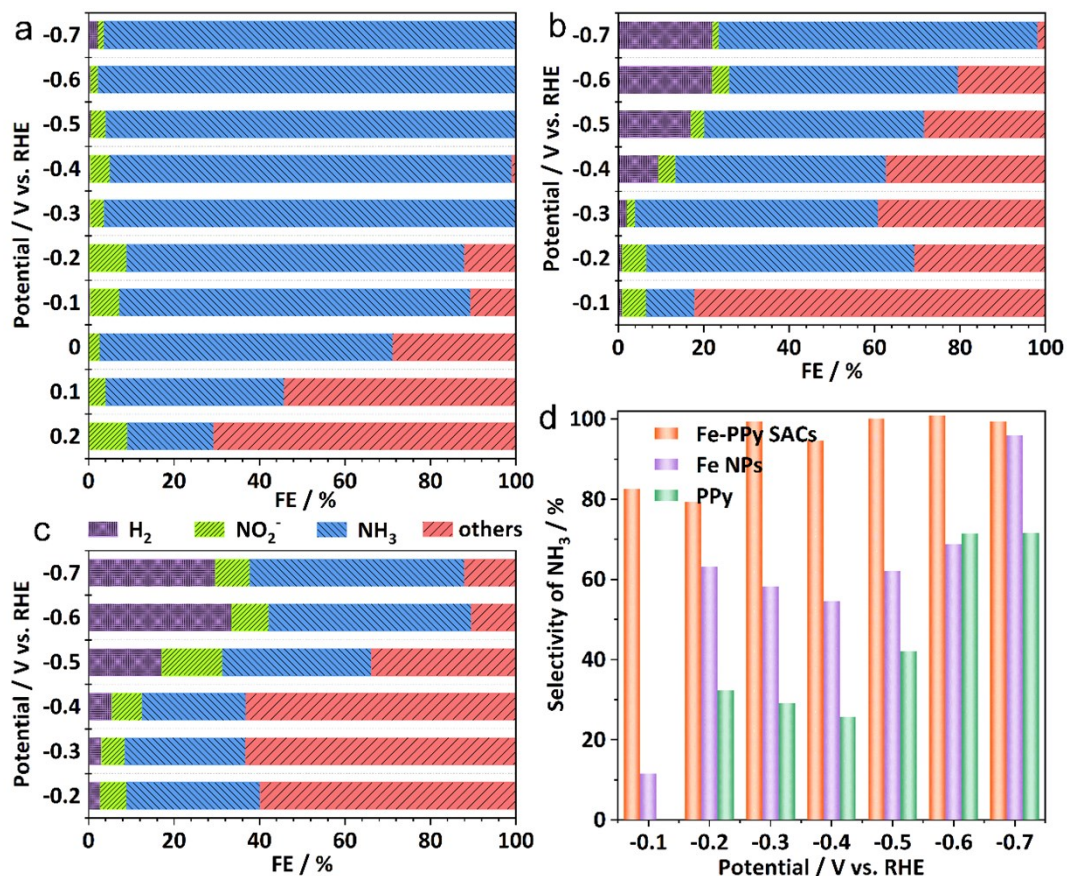


Fig. S10 The faradaic efficiency of H₂, NO₂⁻, NH₃, and other products on (a) Fe-PPy SACs, (b) Fe NPs, and (c) PPy. (d) The selectivity of ammonia of three catalysts.

NO₂⁻ quantification is based on the Griess agent as described in the Experimental Section. H₂ is quantified by a typical substrate generation-tip collection experiment using the SECM (Fig. S9). The F.E. of other gas products (e.g. N₂, N₂H₄, NO₂ etc.), which are most likely to be produced at very low yield though, is defined as the remaining percentage apart from F.E.(NH₃), F.E.(NO₂⁻), and F.E.(H₂). One impressive finding is that almost no H₂ (F.E. < 2%) was detected in Fe-PPy SACs. In contrast, Fe NPs and PPy appear to experience the noticeable H₂ evolution starting from -0.3 V, reaching a highest F.E.(H₂) of ca. 22% and ca. 35%, respectively. It should be further noticed that current densities at potential above 0 V are too low (microamp level) that the quantification of other products, F.E.(others), based on the total charge may remain significant deviations. The majority of the deviations, as far as we are concerned, are probably induced by background signals, double-layered charging current, and instrumental offset, which would not contribute to any faraday reactions. Despite of this, we also contained these unavoidable impacts into the estimation of F.E.(others), but the statement about the accuracy especially for the lower overpotentials as discussed needs careful attention. Consequently, the selectivity of ammonia for the NitRR is compared from -0.1 to -0.7 V (vs. RHE) in Fig. S10, where Fe-PPy SACs reveal the impressively selective NH₃ production with above 80% at all potentials.

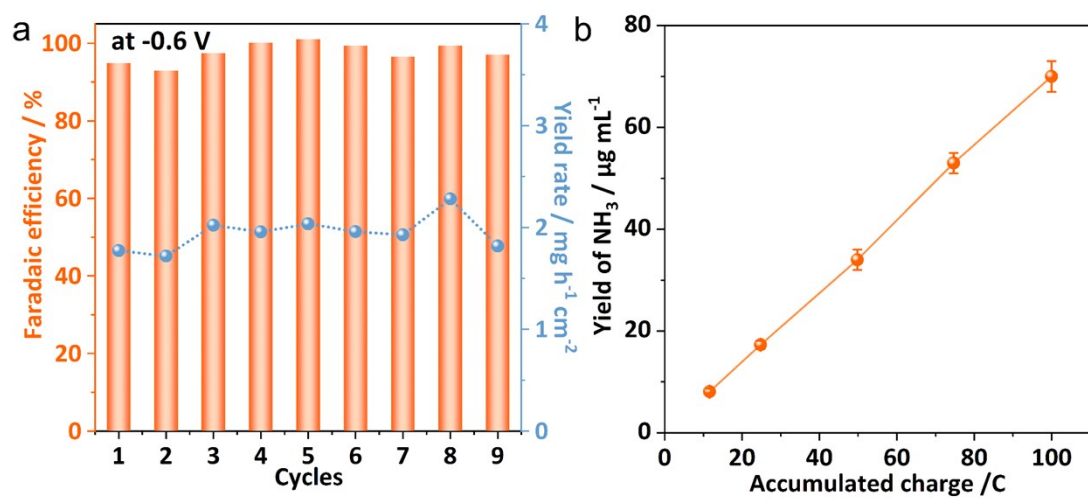


Fig. S11 (a) The catalytic durability of Fe-PPy SACs. (b) The NH_3 yield along with the accumulated charge.

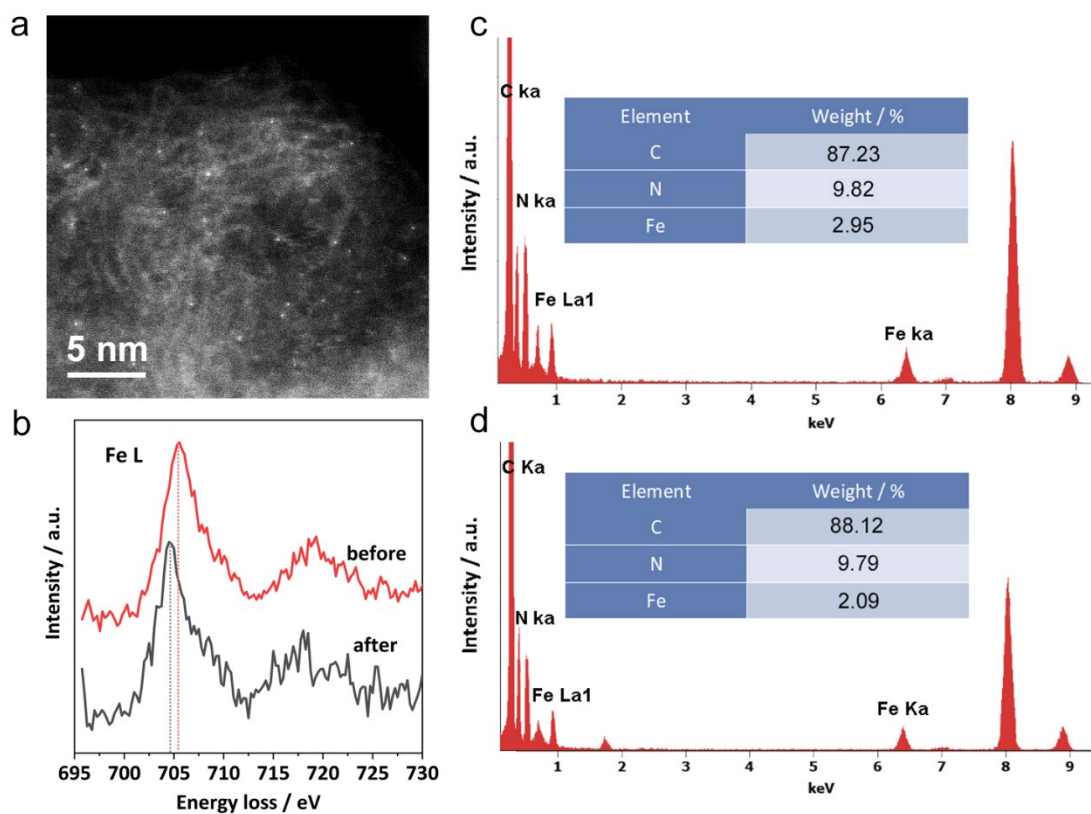


Fig. S12 (a) The STEM of Fe-PPy SACs after the electrolysis. (b) Fe L EELS spectra of Fe-PPy SACs before and after electrolysis. The EDS elemental analysis of Fe-PPy SACs before (c) and after (d) electrolysis.

Fe L EELS (Fig. S12b) and EDS (Fig. S12c-d) images before and after electrolysis (0.5 h at -0.6 V) were carried out to confirm the stability of Fe-PPy SACs in terms of structure and elemental content. A slight negative shift of energy loss was observed on Fe L EELS after electrolysis, suggesting the partial reduction of Fe species due to the negative potential applied on the Fe-PPy SACs.¹⁷ The EDS elemental analysis indicates Fe, N, and C are almost stable before and after electrolysis.

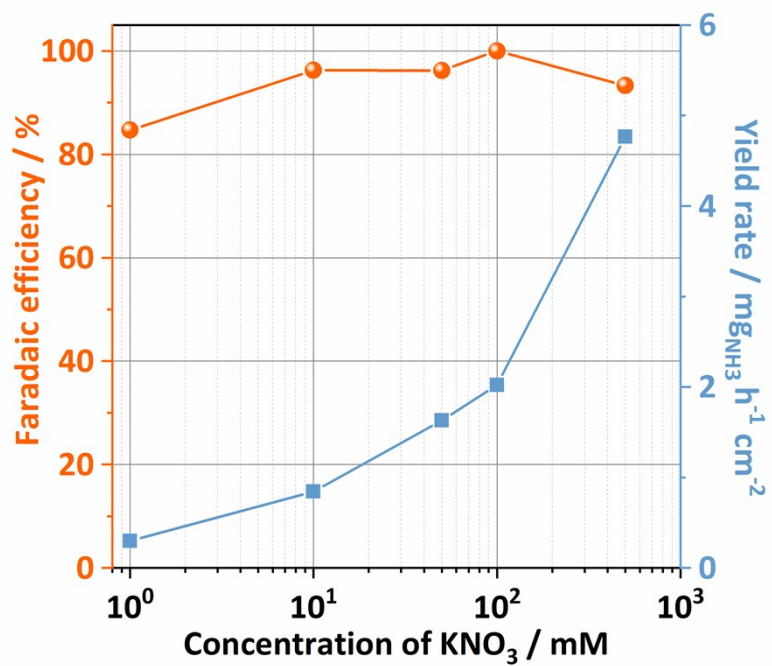


Fig. S13 The faradaic efficiency and yield rate of ammonia in various KNO₃ electrolytes ranged from 1-500 mM.

Table S2 The essential parameters of ammonia synthesis of Fe-PPy SACs compared with other catalysts.

NH ₃ synthesis route	Catalysts	Electrolytes	Mass loading / mg cm _{geo} ⁻²	Yield rate / mmol g ⁻¹ h ⁻¹	Yield rate / μmol cm ⁻² h ⁻¹	Selectivity or faradaic efficiency / %	Energy consumption / kWh kg _{NH₃} ⁻¹	Energy efficiency / %	Ref.
Haber-Bosch	Ru	-	-	60.4	-	66	9	61	18
Enzymatic N ₂ fixation	ATP-nitrogenase	-	-	59	-	-	-	-	19
Photocatalytic N ₂ RR	Modified C ₃ N ₄	N ₂ -saturated EG	10 mg in 40 mL EG	3.42	-	-	12151	-	20
	Mo-PCN SACs	N ₂ -saturated DI water	3 mg (~0.01 mg Mo) in 6 mL DI water	239	-	-	1893	0.6	21
Electrocatalytic N ₂ RR	Ru SACs on N-doped carbon Bi nanocrystals	N ₂ -saturated 0.05 M H ₂ SO ₄	0.255 (0.18% Ru)	7.11	0.0033	29.6	6.76	23.60	22
	MoN@NC	N ₂ -saturated 0.5 M K ₂ SO ₄	0.258	200	51.6	66	8.66	41.11	23
	Zr-TiO ₂	N ₂ -saturated 0.1 M HCl	0.4	4.52	1.81	6.9	6.76	5.50	24
	Bi ₄ O ₁₁ /CeO ₂	N ₂ -saturated 0.1 M KOH	1	0.52	0.52	17.3	7.95	11.74	25
	s-TiO ₂ NTs	N ₂ -saturated 0.1 M HCl	2	1.37	2.74	10.16	6.76	8.10	26
				0.33	1	0.33	26	8.18	17.13
Electrocatalytic NitRR	Strained Ru nanoclusters	1 M KOH + 1 M KNO ₃	0.185	5560	1029	~100	25.60	26.6	28
	Cu-Ni alloy	1 M KOH + 0.1 M KNO ₃	-	-	4160	~100	17.41	29.71	29
	Cu/Cu ₂ O nanowire arrays	0.5 M Na ₂ SO ₄ + 200 ppm nitrate N (NaNO ₃)	-	-	240	81.2	26.23	16.01	30
	O-Cu-PTCDA	PBS (0.1 M, pH = 7) + 500 ppm KNO ₃	0.197 (Cu)	130	25.6	77	20.56	19.37	31
	Au/C	0.5 M K ₂ SO ₄ + 1 mM KNO ₃	0.07	22.63	1.58	26	19.30	6.97	32
	O-TiO ₂ NTs	0.5 M Na ₂ SO ₄ + 50 ppm nitrate N (NaNO ₃)	1	45	45	87.1	27.41	16.43	33
	Fe-PPy SACs	0.1 M KOH + 0.1 M KNO ₃	0.24 (2.38% Fe)	2507 (-0.3 V) 5930 (-0.4 V) 12800 (-0.5 V) 20780 (-0.6 V) 28400 (-0.7 V)	14.32(-0.3 V) 33.87 (-0.4 V) 73.11 (-0.5 V) 118.70 (-0.6 V) 162.22 (-0.7 V)	99.69 (-0.3 V) 94.15 (-0.4 V) 100 (-0.5 V) 100 (-0.6 V) 98.43 (-0.7 V)	19.33 (-0.3 V) 20.60 (-0.4 V) 21.86 (-0.5 V) 23.12 (-0.6 V) 24.38 (-0.7 V)	35.12 (-0.3 V) 31.13 (-0.4 V) 31.46 (-0.5 V) 29.57 (-0.6 V) 27.50 (-0.7 V)	This work

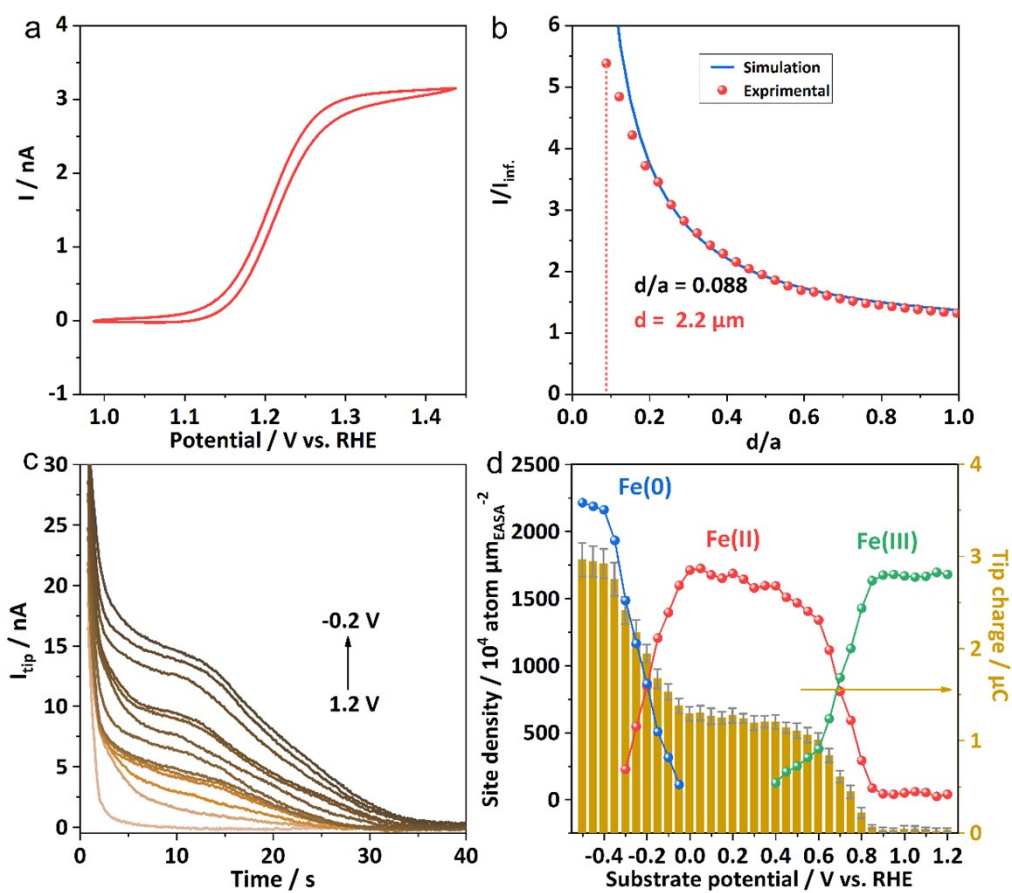


Fig. S14 (a) CV curve of FcMeOH (0.5 mM) oxidation in 0.1 M KOH on a Pt UME (50 μm in diameter). (b) The tip approaching curve to determine the inter-electrode distance (d , ca. 2.2 μm) between the tip and substrate electrodes, where a is the semidiameter of Pt UME (25 μm). (c) The titration curves collected on the tip UME at various substrate potentials for Fe NPs. (d) The site densities of Fe(III), Fe(II), and Fe(0) species on Fe NPs calculated from the tip charge.

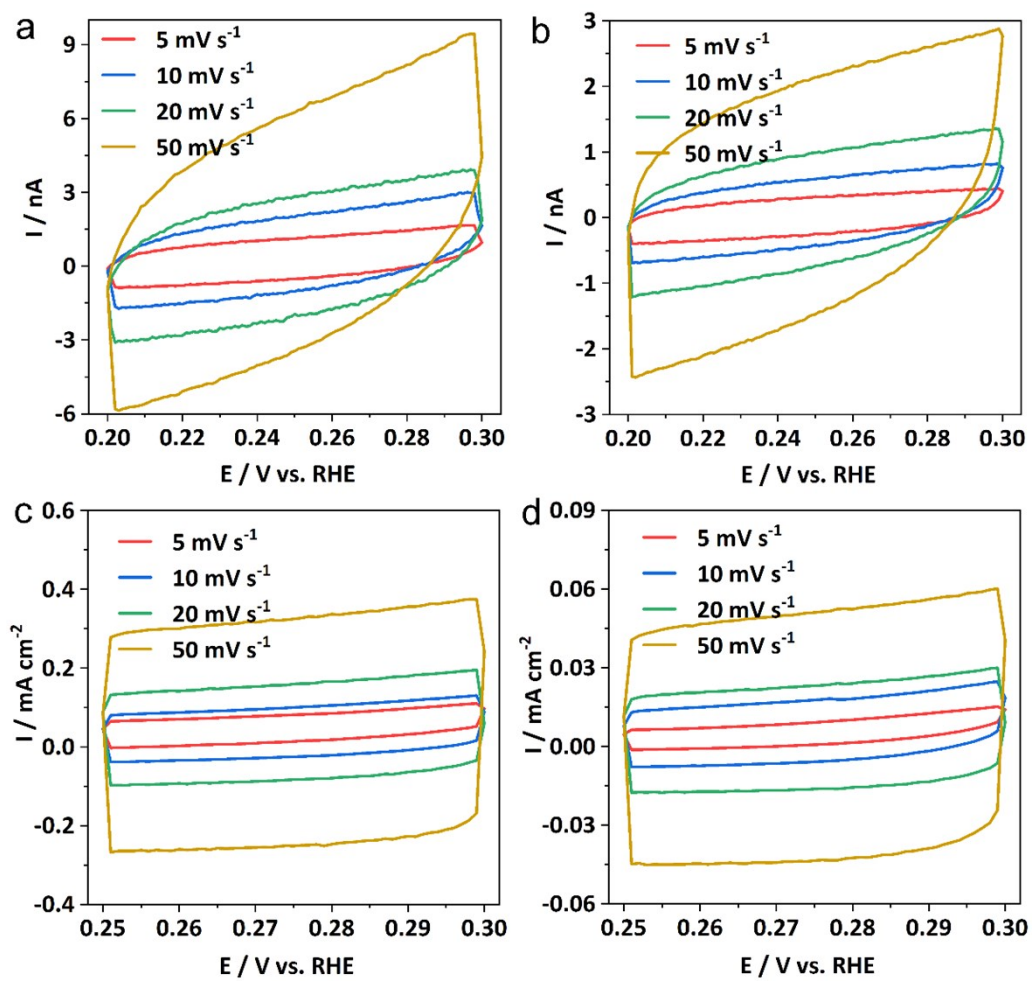


Fig. S15 CVs at different scan rates for determining EASA. (a, c) Fe NPs; (b, d) Fe-PPy SACs.

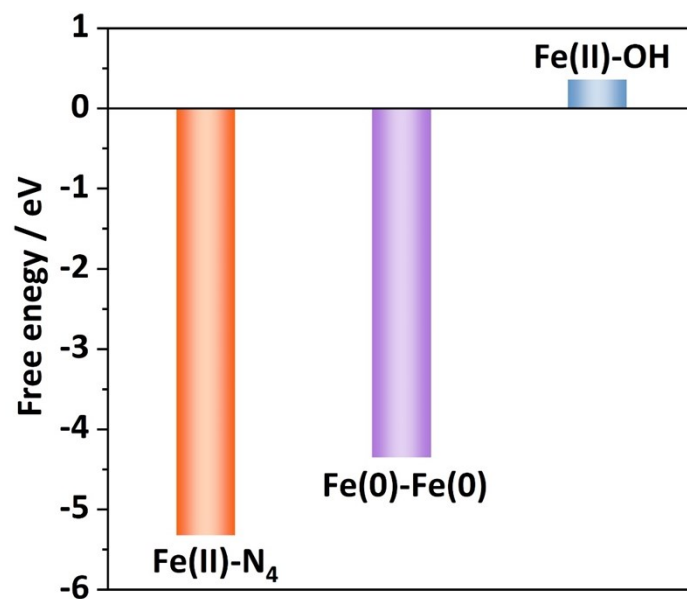


Fig. S16 The free energy of NO_3^- adsorption on Fe-PPy SACs (Fe(II)-N_4), Fe NPs (Fe(0)-Fe(0)), and Fe(OH)_2 (Fe(II)-OH).

Reference

1. A. J. Bard and M. V. Mirkin, in *Scanning Electrochemical Microscopy, Second Edition*, CRC Press, Boca Raton, 2012.
2. B. Zhang, Y. Zhang and H. S. White, *Anal. Chem.*, 2004, **76**, 6229-6238.
3. J. Kwak and A. J. Bard, *Anal. Chem.*, 1989, **61**, 1221-1227.
4. L. C. Green, D. A. Wagner, J. Glogowski, P. L. Skipper, J. S. Wishnok and S. R. Tannenbaum, *Anal. Biochem.*, 1982, **126**, 131-138.
5. D. Zhu, L. Zhang, R. E. Ruther and R. J. Hamers, *Nat. Mater.*, 2013, **12**, 836-841.
6. C. M. Sánchez-Sánchez, J. Rodríguez-López and A. J. Bard, *Anal. Chem.*, 2008, **80**, 3254-3260.
7. B. Delley, *J. Chem. Phys.*, 1990, **92**, 508-517.
8. B. Delley, *J. Chem. Phys.*, 2000, **113**, 7756-7764.
9. S. Grimme, J. Antony, S. Ehrlich and H. Krieg, *J. Chem. Phys.*, 2010, **132**, 154104.
10. S. Grimme, *J. Comput. Chem.*, 2004, **25**, 1463-1473.
11. B. Delley, *Mol. Simul.*, 2006, **32**, 117-123.
12. A. Klamt and G. Schüürmann, *J. Chem. Soc., Perkin Trans. 2*, 1993, DOI: 10.1039/P29930000799, 799-805.
13. E. Skúlason, T. Bligaard, S. Gudmundsdóttir, F. Studt, J. Rossmeisl, F. Abild-Pedersen, T. Vegge, H. Jónsson and J. K. Nørskov, *Phys. Chem. Chem. Phys.*, 2012, **14**, 1235-1245.
14. J. B. Allen and R. F. Larry, *Electrochemical methods fundamentals and applications*, John Wiley & Sons, 2001.
15. D. Reyter, D. Bélanger and L. Roué, *Electrochim. Acta*, 2008, **53**, 5977-5984.
16. Y.-J. Shih, Z.-L. Wu, Y.-H. Huang and C.-P. Huang, *Chem. Eng. J.*, 2020, **383**, 123157.
17. M. S. Thompson, T. J. Zega, P. Becerra, J. T. Keane and S. Byrne, *Meteorit. Planet. Sci.*, 2016, **51**, 1082-1095.
18. M. Kitano, Y. Inoue, M. Sasase, K. Kishida, Y. Kobayashi, K. Nishiyama, T. Tada, S. Kawamura, T. Yokoyama, M. Hara and H. Hosono, *Angew. Chem. Int. Ed.*, 2018, **57**, 2648-2652.
19. F. Simpson and R. Burris, *Science*, 1984, **224**, 1095-1097.
20. W. Wang, H. Zhang, S. Zhang, Y. Liu, G. Wang, C. Sun and H. Zhao, *Angew. Chem. Int. Ed.*, 2019, **58**, 16644-16650.
21. X.-W. Guo, S.-M. Chen, H.-J. Wang, Z.-M. Zhang, H. Lin, L. Song and T.-B. Lu, *J. Mater. Chem. A*, 2019, **7**, 19831-19837.
22. Z. Geng, Y. Liu, X. Kong, P. Li, K. Li, Z. Liu, J. Du, M. Shu, R. Si and J. Zeng, *Adv. Mater.*, 2018, **30**, 1803498.
23. Y.-C. Hao, Y. Guo, L.-W. Chen, M. Shu, X.-Y. Wang, T.-A. Bu, W.-Y. Gao, N. Zhang, X. Su, X. Feng, J.-W. Zhou, B. Wang, C.-W. Hu, A.-X. Yin, R. Si, Y.-W. Zhang and C.-H. Yan, *Nat. Catal.*, 2019, **2**, 448-456.
24. X. Yang, F. Ling, J. Su, X. Zi, H. Zhang, H. Zhang, J. Li, M. Zhou and Y. Wang, *Appl. Catal., B*, 2020, **264**, 118477.
25. N. Cao, Z. Chen, K. Zang, J. Xu, J. Zhong, J. Luo, X. Xu and G. Zheng, *Nat. Commun.*, 2019, **10**, 2877.
26. C. Lv, C. Yan, G. Chen, Y. Ding, J. Sun, Y. Zhou and G. Yu, *Angew. Chem. Int. Ed.*, 2018, **57**, 6073-6076.
27. P. Li, Z. Jin, Z. Fang and G. Yu, *Angew. Chem. Int. Ed.*, 2020, **59**, 22610-22616.
28. J. Li, G. Zhan, J. Yang, F. Quan, C. Mao, Y. Liu, B. Wang, F. Lei, L. Li, A. W. M. Chan, L. Xu, Y. Shi, Y.

- Du, W. Hao, P. K. Wong, J. Wang, S.-X. Dou, L. Zhang and J. C. Yu, *J. Am. Chem. Soc.*, 2020, **142**, 7036-7046.
29. Y. Wang, A. Xu, Z. Wang, L. Huang, J. Li, F. Li, J. Wicks, M. Luo, D.-H. Nam, C.-S. Tan, Y. Ding, J. Wu, Y. Lum, C.-T. Dinh, D. Sinton, G. Zheng and E. H. Sargent, *J. Am. Chem. Soc.*, 2020, **142**, 5702-5708.
30. Y. Wang, W. Zhou, R. Jia, Y. Yu and B. Zhang, *Angew. Chem. Int. Ed.*, 2020, **59**, 5350-5354.
31. G.-F. Chen, Y. Yuan, H. Jiang, S.-Y. Ren, L.-X. Ding, L. Ma, T. Wu, J. Lu and H. Wang, *Nat. Energy*, 2020, **5**, 605-613.
32. J. Choi, H.-L. Du, C. K. Nguyen, B. H. R. Suryanto, A. N. Simonov and D. R. MacFarlane, *ACS Energy Lett.*, 2020, **5**, 2095-2097.
33. R. Jia, Y. Wang, C. Wang, Y. Ling, Y. Yu and B. Zhang, *ACS Catal.*, 2020, **10**, 3533-3540.